In situ unraveling surface reconstruction of Ni-CoP nanowire for excellent alkaline water electrolysis

Haiquan Liu[1], Sihang Hu[1], Baojun Long[1], Huan Dai[1], Yafei Yang[1], Menghua Yang[1], Qi Zhang[1], Zunjian Ke[1], Wenqing Li[1], Dong He[1], Ziyu Wang[1], and Xiangheng Xiao[1]

[1]Wuhan University

August 21, 2024

Abstract

The surface reconstruction behavior of transition metal phosphides (TMPs) precursors is considered an important method to prepare efficient oxygen evolution catalysts, but there are still significant challenges in guiding catalyst design at the atomic scale. Here, the CoP nanowire with excellent water splitting performance and stability is used as a catalytic model to study the reconstruction process. Obvious double redox signals and valence evolution behavior of the Co site are observed, corresponding to Co2+/Co3+ and Co3+/Co4+ caused by auto-oxidation process. Importantly, the in-situ Raman spectrum exhibits the vibration signal of Co-OH in the non-Faradaic potential interval for oxygen evolution reaction, which is considered the initial reconstruction step . Density functional theory and ab initio molecular dynamics are used to elucidate this process at the atomic scale: First, OH- exhibits a lower adsorption energy barrier and proton desorption energy barrier at the configuration surface, which proposes the formation of a single oxygen group. Under a higher -O group coverage, the Co-P bond is destroyed along with the POx groups. Subsequently, lower P vacancy formation energy confirm that the Ni-CoP configuration can fast transform into highly active phase. Based on optimized reconstruction behavior and rate-limiting barrier, the Ni-CoP exhibit an excellent overpotential of 236 mV for OER and 1.59 V for overall water splitting at 10 mA cm-2, which demonstrates low degradation (2.62 %) during the 100 mA cm-2 for 100 h. This work provide systematic insights into the atomic-level reconstruction mechanism of TMPs, which benefit further design of water splitting catalyst.

Article category: Research Article

Subcategory: Electrocatalyst

In situ unraveling surface reconstruction of Ni-CoP nanowire for excellent alkaline water electrolysis

Haiquan Liu[1,2], Sihang Hu[2], Baojun Long[2], Huan Dai[2], Yafei Yang[2], Menghua Yang[2], Qi Zhang[2], Zunjian Ke[2], Wenqing Li[2], Dong He[2,], Ziyu Wang[1,*] & Xiangheng Xiao[2,*]*

Affiliations

[1] The Institute of Technological Sciences, Wuhan University, Wuhan 430072, Hubei, China

[2] School of Physics and Technology, Zhongnan Hospital of Wuhan University, Wuhan University, Wuhan 430072, Hubei, China

***Corresponding Author**

Dr. Dong He; School of Physics and Technology, Zhongnan Hospital of Wuhan University, Wuhan University, Wuhan 430072, Hubei, China; hedong@whu.edu.cn

Prof. Dr. Ziyu Wang; The Institute of Technological Sciences, Wuhan University, Wuhan 430072, Hubei, China; zywang@whu.edu.cn

Prof. Dr. Xiangheng Xiao; School of Physics and Technology, Zhongnan Hospital of Wuhan University, Wuhan University, Wuhan 430072, Hubei, China; xxh@whu.edu.cn

Abstract

The surface reconstruction behavior of transition metal phosphides (TMPs) precursors is considered an important method to prepare efficient oxygen evolution catalysts, but there are still significant challenges in guiding catalyst design at the atomic scale. Here, the CoP nanowire with excellent water splitting performance and stability is used as a catalytic model to study the reconstruction process. Obvious double redox signals and valence evolution behavior of the Co site are observed, corresponding to $Co^{2+}/Co^{3+}$and Co^{3+}/Co^{4+} caused by auto-oxidation process. Importantly, the in-situ Raman spectrum exhibits the vibration signal of Co-OH in the non-Faradaic potential interval for oxygen evolution reaction, which is considered the initial reconstruction step. Density functional theory and ab initio molecular dynamics are used to elucidate this process at the atomic scale: First, OH^- exhibits a lower adsorption energy barrier and proton desorption energy barrier at the configuration surface, which proposes the formation of a single oxygen (-O) group. Under a higher -O group coverage, the Co-P bond is destroyed along with the PO_x groups. Subsequently, lower P vacancy formation energy confirm that the Ni-CoP configuration can fast transform into highly active phase. Based on optimized reconstruction behavior and rate-limiting barrier, the Ni-CoP exhibit an excellent overpotential of 236 mV for OER and 1.59 V for overall water splitting at 10 mA cm^{-2}, which demonstrates low degradation (2.62 %) during the 100 mA cm^{-2} for 100 h. This work provide systematic insights into the atomic-level reconstruction mechanism of TMPs, which benefit further design of water splitting catalysts.

Keywords

Surface reconstruction, In situ Raman spectra, Oxygen evolution reaction, Transition metal phosphides, Phase transformation

1. Introduction

In recent years, electrocatalytic water splitting has been recognized as a reliable way to produce green hydrogen in the field of energy conversion, which can help alleviate environmental problems caused by fossil energy[1,2]. However, the water splitting reaction is severely inhibited by the four-electron transfer process corresponding to the anode oxygen evolution reaction (OER), which makes it urgent to explore catalysts with suitable cost and activity to optimize the overall reaction rate[3,4]. Ruthenium/iridium-based noble metal catalysts have demonstrated excellent catalytic activity in alkaline OER, but large-scale application strategies are limited by high cost and low stability[5-8]. As typical representatives of non-noble metal materials, transition metal-based oxides (hydroxides), phosphides and selenides can optimize the adsorption/desorption behavior and rate-limiting step free energy of oxygen intermediates, which alleviates energy consumption issues in the green hydrogen production process[9-13]. Importantly, the above catalytic configuration is often accompanied by surface reconstruction behavior under operating conditions, which leads to the transformation of the original configuration into a hydrogen oxide phase or a superoxide phase. Therefore, it is necessary to comprehensively understand the intrinsic reconstruction kinetics of catalytic configurations in water electrolysis reactions, which can help distinguish real active phases and design more valuable structure-activity relationships.

Compared with transition metal oxides (TMOs), the quasi-covalent bridging mode between metal and non-metal site in transition metal phosphides (TMPs) leads to excellent conductivity and water splitting activity, but complex reconstruction behavior is difficult to be visually observed at the atomic scale[14-19]. Although the terminal reconstruction configuration of TMPs is also considered to be oxyhydroxide or superoxide, but the evolution behavior of phosphorus species during the initial reconstruction process has not been fully elucidated, which is crucial for regulating the generation behavior of the active phase[20-22]. In addition, the impact of the charge redistribution effect introduced by the doping strategy on the important reconstruction process has not been elucidated from a theoretical level, which ignores the complex interaction between phosphorus species and oxygen species[23-25]. Considering that the interaction between lattice phosphorus and

oxygen adsorbed species plays an important driving role in the overall reconstruction, which urgently requires the combination of in-situ spectroscopic characterization methods, thermodynamic theoretical calculations, and molecular dynamics simulations to comprehensively provide the internal connection between hybrid structure and configuration evolution process.

In this work, CoP nanowires prepared by hydrothermal-phosphating method were used as catalyst models, which has demonstrated excellent water-splitting activity and long-term stability. Typical double oxidation peaks are found in the cyclic voltammetry (CV) curve of NiCoP nanowires, which combined with quasi in-situ X-ray photoelectron spectroscopy (XPS) are identified as the autoxidation behavior of metal sites, including Co^{2+}/Co^{3+} and Co^{3+}/Co^{4+}. Interestingly, the typical vibrational mode of $Co(OH)_2$ in the in situ Raman spectrum is found at 0.7 V vs RHE, indicating that the initial reconstruction behavior of the CoP system can be driven by a lower non-Faradaic potential. Based on adsorption-desorption thermodynamics and kinetics, density functional theory (DFT), ab initio molecular dynamics (AIMD) simulations and in situ spectroscopic characterization intuitively provide the configuration evolution process of CoP-based catalysts from the atomic scale, which mainly includes: OH^- adsorption, spontaneous proton desorption, P-O coordination, destroyed Co-P bond, Co-OH, Co-O, Co-OOH and Co-OO (Figure 1a). In addition, the reconstruction process of CoP can be significantly promoted by the heteroatom Ni, which mainly reduces the formation energy of P vacancies. Summary, the initial reconstruction behavior and phase transition regulation mechanism of typical CoP model were studied, which provides novel insights into the advanced reconstruction-activity relationships of water electrolysis catalysts.

2. Results and discussion

2.1. Synthesis and Structural Characterizations

As a catalytic model, CoP-based nanowires were uniformly prepared on the surface of carbon cloth (CC) through a hydrothermal-phosphating method (Figure S1). X-ray diffraction (XRD) patterns exhibit an orthorhombic phase of CoP-based nanowires with space group Pnma (62), well matched with CoP (PDF#29-497) (Figure S2)[26,27]. Compared with CoP, the individual diffraction signals of Ni-CoP are slightly shifted towards low Bragg diffraction angles, implying that the heteroatom Ni is successfully incorporated into CoP (Figure S2a). According to scanning electron microscope (SEM) and high angle annular dark field (HAADF), the CC fibers are coated by Ni doped CoP nanowires with an average length 2 μm, which still maintains the nanowire shape of precursor (Figure 1b and Figure S3 and Figure S4). The high-resolution TEM (HR-TEM) images of Ni-CoP indicate lattice fringes of 0.241 nm and 0.249 nm, corresponding to the (102) and (111) planes (Figure 1c)[28]. The constituent elements of CoP and Ni-CoP are uniformly distributed on the nanowires, and TEM-energy dispersive spectrometer (TEM-EDS) confirm that the constituent elements basically meet the reagent dosage ratio in the experimental strategy (Figure 1b and Figure S5a-c). The bright diffraction rings are exhibited in selected area electron diffraction (SAED) patterns of CoP and Ni-CoP nanowires, corresponding to (011), (111), (112) and (020), which is consistent with the preferred orientation in the XRD pattern (Figure S5d,e).

XPS and X-ray absorption spectroscopy (XAS) were used to further analyze the elemental composition and electron population of the CoP-based catalyst, which provided the control behavior of various heteroatoms on the original electronic structure. The constituent elements of CoP and Ni-CoP are observed in XPS, which is corroborated by the TEM-EDS image (Figure S6a). In the Co 2p spectra of CoP, the double peaks appearing at 779.05 and 794.25 eV are attributed to Co-P bond (Figure 1d). The peaks centered at 782.22 and 798.68 eV and two satellite peaks obtained at 788.21 and 804.19 eV can be attributed to Co-PO_xresulting from oxygen group adsorption behavior. In addition, peak signals in the high-resolution P 2p spectrum are found at 129.29 eV and 130.17 eV, corresponding to P $2p_{3/2}$ and P $2p_{1/2}$ (Figure S6b). The peak signal provided by the P-O bond is observed at 134.3 eV. The electronegativities Ni are 1.91, which are higher than that of Co (1.88)[29,30]. The heteroatom Ni in CoP lattice causes electrons to transfer from Co to Ni, leading to the positively shift in binding energy. Hence, compared with the typical peak signal of CoP, Co 2p and P 2p signal of Co site in Ni-CoP is positively shifted, which is located at electron loss region. Synchrotron radiation-based soft XAS was used to further determine the modulation behavior of the heteroatom Ni on

the charge population around the Co site. The Co L-edge XAS spectra of CoP nanowire are divided into L_3-edge (780.33 ~ 783.68 eV) and the L_2-edge (795.88 ~ 798.19 eV) (Figure 1e). Besides, slight shoulder signals are observed near Co $L_{2,3}$-edge peaks, which are attributed to two coordination environments around the Co site, including to Co-P and Co-PO_x bond. Obvious absorption peaks are found at 136.87 ~ 139.23 eV and 146.84 eV, which correspond to the P 2p signal in CoP (Figure S6c). The positive shift behavior of Co and P L-edge affected by heteroatom Ni confirm the Co 2p and P 2p in XPS. Further, the soft XAS peaks are located at approximately 854.9 eV (L_3-edge) and 873.24 eV (L_2-edge), corresponding the electron redistribution from Ni $2p_{3/2}$and $2p_{1/2}$ to 3d orbitals, which means the successful incorporation of Ni heteroatoms into the CoP lattice (Figure S6d,e). The initial reconstruction behavior and the rate-limiting energy barrier can be controlled by the charge redistribution effect between the heteroatom Ni and Co sites, which will be introduced in the theoretical calculations.

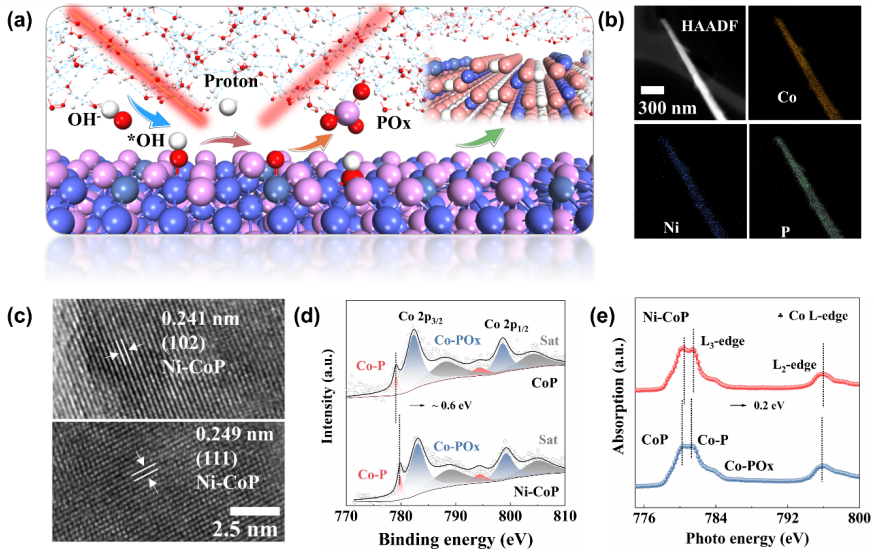

Figure 1. a) In situ characterization and surface reconstruction processes of transition metal phosphides. b) HRTEM-HAADF and element distribution of the Ni-CoP. c) HRTEM images of Ni-CoP. d) High resolution XPS-Co 2p and e) soft XAS-Co L-edge of CoP and Ni-CoP.

2.2. Alkaline water splitting properties

An important limiting factor in the water splitting reaction rate and energy consumption is the anode OER[31-33]. Therefore, anode catalysts with excellent performance and stability are required to achieve efficient green hydrogen production. Covalent-like bonding mode between transition metal sites and non-metal sites in CoP-based catalyst can lead to excellent thermodynamic behavior and conductivity. The electrochemical OER properties of CoP-based catalysts were studied in the electrolyte solution 1 M KOH, which exhibits lower overpotentials of 236, 287, and 291 mV to reach 10, 150 and 300 mA cm^{-2}, respectively (Table S1, Figure 2a and Figure S7a,b). Such overpotential is competitive among the other Co-based phosphide or noble metal catalysts reported in the related reference (Table S2 and Figure S7c). The Tafel slope and R_{ct} of Ni-CoP nanowire are fitted as 52.55 mV dec^{-1} and 1.80 Ω, which is much lower than that of other M-CoP catalyst and 6 mg-commercial catalysts (Figure 2b, Figure S7d-f). The above results indicate that Ni-CoP nanowire has excellent reaction kinetics and charge transport behavior. In addition, the double layer capacitor (C_{dl}) of sample are calculated as 698.84 (CoP), 680.51 (Cr-CoP), 621.43 (Fe-CoP) and 538 mF cm^{-2} (Ni-CoP) (Figure S8a-d). The linear scanning voltammetry (LSV) curves of all samples are normalized by C_{dl}, which is purposed to study the intrinsic catalytic activity. The normalized LSV curves exhibit that OER performance of Ni-CoP nanowires is still better than that of CoP and other M-CoP nanowires (Figure S8e,f). To explore the relationship between heteroatom Ni content and catalytic performance, the heteroatom

Ni doping content is controlled by the molar ratio between nickel nitrate and cobalt nitrate, which has been described in the experimental part. Similar to Ni-CoP-0.1 mmol, CoP nanowires with different heteroatom Ni content (0.15 mmol and 0.2 mmol) are successfully prepared in CC, which was confirmed in SEM and XRD (Figure S9). Compared with Ni-CoP-0.15 mmol and 0.2 mmol, Ni-CoP-0.1 mmol nanowire still exhibit the smallest overpotential at 10, 150 and 300 mA cm^{-2}, which indicate most excellent OER performance (Table S3 and Figure S10).

Similarly, three-electrode system was used to analyze the hydrogen evolution reaction (HER) activity of CoP-based catalysts in 1 M KOH. The Ni-CoP nanowire with superior HER performance still exhibits lower overpotential at 100, 200 and 400 mA cm^{-2}, which is 99, 163 and 298 mV lower than that of bare CoP, respectively (Table S4, Figure 2c and Figure S11b). Specific current density can be achieved by Ni-CoP at lower applied potentials, which are significantly better than bare CC, Co(OH)F, CoP, other M-CoP nanowires, commercial Pt/C and other TMPs-based catalysts (Table S5, Figure S11a,c). The Tafel slope of Ni-CoP (40.54 mV dec^{-1}) is much smaller than CoP (63.17 mV dec^{-1}), commercial Pt/C (67.82 mV dec^{-1}) and other M-CoP nanowires, revealing that the HER kinetic are accelerated by heteroatom Ni (Figure S11d). The Ni-CoP nanowires with lower Tafel slope and charge transfer resistance (R_{ct} = 1.837 Ω) exhibit ultrafast reaction kinetics based on Volmer-Heyrovsky mechanism during HER (Figure S11e,f). The C_{dl} of CoP, Cr-CoP, Fe-CoP and Ni-CoP nanowires are calculated to be 35.34 mF cm^{-2}, 29.38 mF cm^{-2}, 20.39 mF cm^{-2} and 19.94 mF cm^{-2}, respectively (Figure S12a-d). Besides, the normalized LSV curves of Ni-CoP nanowire has the most excellent catalytic activity, which originates from the regulation behavior of heteroatom Ni on the electronic structure around Co sites (Figure S12e,f). For relationship between different Ni doping amounts and HER performance, Ni-CoP-0.1 mmol nanowire exhibits the smallest overpotential (at 100, 200, 300 mA cm^{-2}), which imply excellent HER performance compared with other heteroatom contents (Table S6 and Figure S13).

Considering the excellent activity and reaction kinetics exhibited by Ni-CoP nanowires (even better than 6 mg-commercial Pt/C and RuO_2 catalysts), the Ni-CoP nanowire grown on CC were used as cathode/anode in the electrolytic cell (two-electrode), which can directly evaluate the feasibility of the electrolytic water splitting system (Ni-CoP || Ni-CoP) in practical applications. Compared with commercial Pt/C||RuO_2 catalytic system (1.62 V), the Ni-CoP || Ni-CoP electrodes exhibit an excellent overall water splitting performance, which can reach a current density of 10 mA cm^{-2} at 1.59 V (Figure 2d). For other recently reported Co-based bifunctional catalysts, the excellent water-splitting performance exhibited by the Ni-CoP || Ni-CoP catalyst with lower overpotential is still competitive (Table S7 and Figure S14). The chronoamperometric curve collected at current density of 10 mA cm^{-2} demonstrate that the corresponding potential of Ni-CoP || Ni-CoP catalyst failed to show noticeable change for at least 24 h (Figure S15a). In addition, compared with the LSV curves of Ni-CoP nanowires before the stability test, the Ni-CoP nanowire demonstrate superior durability with no obvious attenuation after continuous operation 24 h (Figure S15b). Notably, the SEM images exhibit that the Ni-CoP electrode retains the original nanowire structure even after the HER test. It is worth noting that the Ni-CoP electrode still maintained the pristine nanowire structure after the long-time HER test, which is obviously different from the Ni-CoP electrode after the long-time OER test (inset in Figure 2e). Considering the deep reconstruction phenomenon under long-term working conditions, high-resolution XPS were used to analyze the elemental composition and chemical valence state after the OER stability test (current density = 10 mA cm^{-2}, acquisition time = 24 h). The high-resolution XPS Co 2p peak signals of the double-transition metal active sites in Ni-CoP nanowire are not annihilated by the long-term alkaline oxygen evolution environment, which reveal the fundamental source of the excellent stability (Figure S16a). Subsequently, it can be clearly seen that Co 2p in the high-resolution XPS image is composed of spin-splitting signals introduced by Co^{3+} and Co^{4+}, including Co $2p_{3/2}$, Co $2p_{1/2}$ and satellite peaks. The high-resolution P 2p spectrum exhibits a distinct typical peak introduced by the P-O bond, which is attributed to the re-adsorption behavior of PO_4^{3-} on the catalyst surface (Figure S16b). However, the signals introduced by Co-P bonds in pristine Ni-CoP could not be observed, corresponding to the dissolution process of Ni-CoP at low positive potential. For alkaline OER, OH^- adsorption, proton desorption and electro-oxidation processes are index to accompanying phenomena of the surface reconstruction behavior.

Compared with pristine Ni-CoP, the high-resolution O 1s of Ni-CoP nanowires after the stability test exhibit obvious peaks at 529.59 eV, 530.86 eV, 531.53 eV, and 533.37 eV, which are indexed by lattice oxygen (Co-O), O_2^{2-} species, OH^-group (or V_o) and adsorbed H_2O molecules (Figure S16c). In particular, the signal peak provided by the O_2^{2-} and OH^- group represents the incomplete evolution stage of CoOOH to CoO_2 species, which implies that the OER active phase of Ni-CoP is identified as Ni-CoOOH/CoO_2 species after stability test. Besides, chronopotentiometry curves under multicurrent step and large current density were used to further study the stability of Ni-CoP in water electrolysis reactions. The multicurrent chronopotentiometry curve of Ni-CoP nanowire with the current increasing from 10 to 190 mA cm^{-2} (increase at a rate of 10 mA cm^{-2} per 10 min) (Figure S15c). The stable overpotential can be clearly observed, which undoubtedly further confirms the excellent stability and mass transfer properties (Figure S15d). The long-term stability of Ni-CoP || Ni-CoP system was examined by a constant current chronopotentiometry at the current density of 10 and 100 mA cm^{-2} for 100 h. Compared with previously reported noble metal-based catalysts, the overpotential of the Ni-CoP system only decreased by 0.61% and 2.62% after water splitting reaction for 100 h, which confirms the reference value of the Ni-CoP system in the green hydrogen production process (Figure 2e).

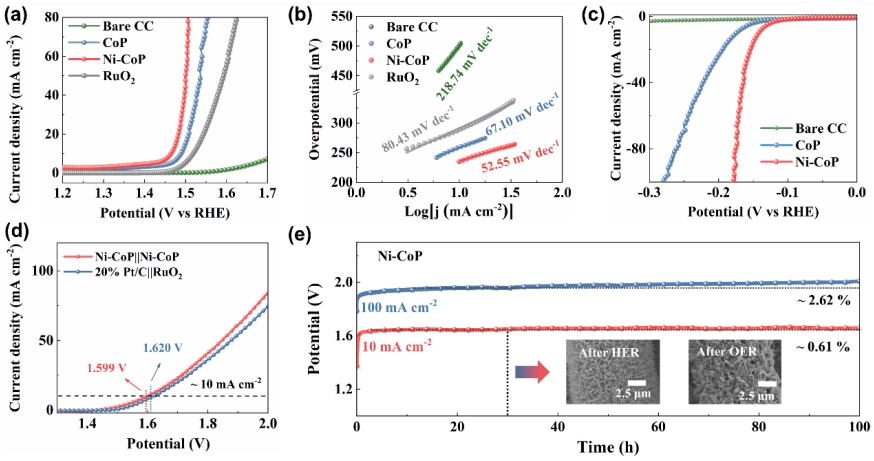

Figure 2. Electrochemical properties of bare CC, CoP, Ni-CoP and RuO_2: a) LSV curves for OER, b) Tafel slope for OER, c) LSV curves for HER. d) Polarization curves of overall water splitting. e) Chronopotentiometry curve of Ni-CoP-0.1 mmol || Ni-CoP-0.1 mmol with a constant current density of 10 and 100 mA cm^{-2} for 100 h.

2.3. Self-reconstruction process and theoretical simulation

The complex reconstruction process of transition metal-based catalysts in alkaline OER processes has always been considered an important issue in the field of water electrolysis. The actual catalytic active phase and configuration evolution mechanism are difficult to identify by traditional spectroscopic characterization, especially the atomic-level evolution kinetics of non-metallic sites in catalyst systems such as phosphide and sulfide. In previous reports, the active phase of transition metal-based sulfide and phosphide in alkaline OER is usually considered to be oxyhydroxide, which fails to intuitively propose a complete evolution path, key thermodynamic steps and regulation method. Here, the CoP-based catalytic configuration with excellent water splitting activity is used as a typical model. The configuration evolution mechanism is systematically studied based on electrochemical characteristic curve coupled in-situ spectroscopy characterization, DFT calculations and AIMD simulations. Double redox peaks were observed in the CV curve of Ni-CoP catalyst, which represents the typical autoxidation behavior of M^{2+}/M^{3+} and M^{3+}/M^{4+} at metal sites, approximately corresponding to 1.1 V and 1.3 V vs RHE (Figure 3a). The valence evolution behavior of the Co site was confirmed in the quasi in-situ high resolution Co 2p spectrum, which gradually changes from Co-PO_X bonding mode to Co^{2+}, Co^{2+}/Co^{3+} and Co^{3+}/Co^{4+} contributed by Co-O bonding mode (Figure 3b). Interestingly,

in situ Raman spectroscopy shows that CoP-based catalysts exhibit vibration signals of hydroxide species at non-Faradic interval, corresponding to the Co-OH configuration, which is obviously different from the reconstruction behavior of traditional oxides (Figure 3c). DFT calculations were used to elucidate the interaction between the lattice P sites and adsorbed oxygen species during the initial reconstruction process from the atomic scale, which demonstrates the lower adsorption (0.068 eV) and proton desorption energy barrier (-0.438 eV) of -OH at the P site (Figure 3e). The above calculation results provide the basic path of the initial reconstruction process from a static thermodynamic perspective, which is mainly the -OH adsorption at the P site followed by the spontaneous proton desorption to form a single oxygen (-O) group. AIMD provides an intuitive initial reconstruction process from the perspective of dynamic simulation, which obviously confirms the results of in-situ Raman spectroscopy and DFT calculations. Interestingly, abundant -O groups are formed by the -OH adsorption process at active sites and spontaneous proton desorption behavior, which is accompanied by P vacancies caused by PO_X coordination and delattice process (Figure 3d). Furthermore, the connection between different surface coverage of -O groups and surface reconstruction is further discussed through AIMD. When the -O group coverage occupies half of the active sites, although P-O bonds are formed, but Co-P bonds are maintained in the original configuration (Figure S17a). Considering that the configured surface is exposed to a richer -OH environment at the anodic potential, the coverage of the -O group is further adjusted from half coverage to full coverage (Figure S17b). The results show that PO_Xcoordination and the breaking behavior of Co-P bonds are positively correlated with the coverage of -O groups, which is accompanied by the generation of P vacancies (Figure 3f and Figure S17c). Therefore, P vacancy is an important intermediate configuration in the initial reconstruction process of TMPs-based catalytic systems in OER. The broken Co-P bond is accompanied by the formation of abundant unsaturated coordination metal sites, which promotes the formation process of the Co-OH intermediate state. Based on reduced Co-P peak area in quasi in-situ high-resolution P 2p spectrum and the stretched Co-O bond provided by AIMD, it can be clearly observed that the interaction between Co and P sites is weakened during the reaction process (Figure S18).

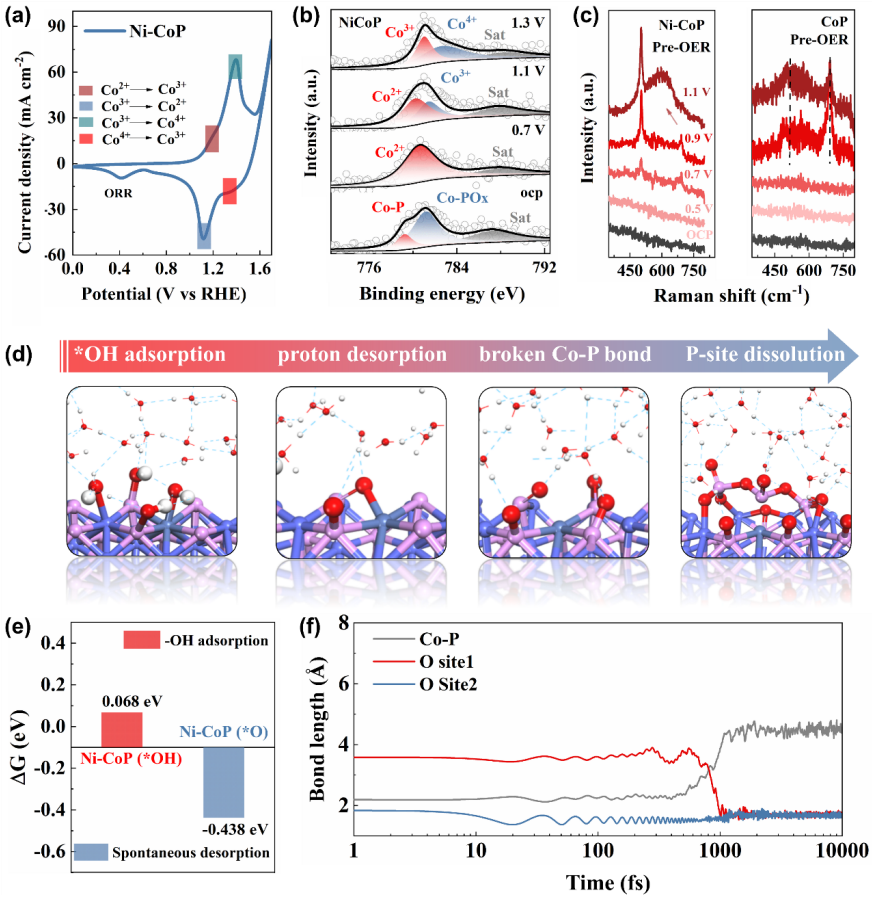

Figure 3. a) CV curves of Ni-CoP at scan rate 20 mV s^{-1} in 1 M KOH. b) Quasi-in situ XPS of Co $2p_{3/2}$ at different applied potentials. c) In-situ Raman spectra for Ni-CoP and CoP collected under multi-potential steps. d) Initial surface reconstruction process of CoP-based catalysts supplied by AIMD. e) The free energy of -OH adsorption and proton desorption at the P site in Ni-CoP. f) Dynamic bond lengths resulting from molecular dynamics processes.

According to in-situ Raman spectroscopy and quasi in-situ high resolution Co 2p/O 2p spectrum, CoP-based catalysts exhibit similar surface reconstruction behavior to TMOs at higher potentials, which corresponds to Co(III)-OOH and Co(IV)-OO species (Figure 4a and Figure S18)[34-38]. Considering the stability of the intermediate state generated by the reconstruction during the OER process, in-situ Raman spectra from high potential (1.5 V vs RHE) to low potential (OCP) were further collected. The vibrational state of superoxide is still can be observed, which means that the intermediate configuration can be maintained during the electrochemical process (Figure S19a). Based on the above discussion, the surface reconstruction pathway of CoP-based catalysts is summarized by the following equation:

Total process: (1)

Co site: (2)

P site (step 1): (3)

P site (step 2): (4)

Based on AIMD and DFT calculations, P vacancies were identified as the key evolution state of TMPs catalysts in the early stages of reconstruction. It is necessary to understand the specific role of doping

strategies in the dissolution process of non-metal sites, which can help to controllably adjust the catalyst reconstruction efficiency and reaction kinetics. Compared with the original CoP configuration, in situ Raman spectrum shows that the reconstructed intermediate state (hydroxide, oxyhydroxide and superoxide species) of the Ni-CoP configuration can be rapidly formed at a lower anode potential (Figure 3c and Figure 4a). In addition, the superoxide phase of the Ni-CoP configuration in time-resolved in-situ Raman spectroscopy can be found at 1.3 V vs RHE, which is 0.2 V lower than the original CoP configuration (Figure S19b). Here, the regulatory effect of heteroatom Ni on the surface reconstruction process of CoP configuration is further analyzed through DFT calculations. It can be clearly observed that the heteroatom Ni can reduce the P vacancy formation energy of the original CoP during the reconstruction process by about 0.2 eV, which means that the Ni-CoP system has efficient initial reconstruction kinetics and metal-oxygen active configuration evolution process (Figure 4b).

Subsequently, DFT calculation are used to further study the regulation effect of heteroatom Ni on the HER/OER performance of CoP configuration. Considering the reconstruction behavior of the CoP-based catalytic model in the anode reaction, the oxyhydroxide model were used to discuss the impact of heteroatom Ni on the OER performance of the original configuration. DFT simulations show that the heteroatom Ni reduces formation energy barrier of key intermediate *OOH by 0.44 eV, which promotes the OER activity of the catalytic configuration by optimizing the rate-limiting step (Figure 4c). For HER, the configuration evolution behavior of CoP and Ni-CoP in 1 M KOH was studied by in situ Raman spectrum, and the vibration signals showed that the CoP-based catalytic surface can still be maintained in alkaline HER (Figure S20). Therefore, the initial CoP and Ni-CoP configurations were used as theoretical models, which further analyzed the influence of heteroatom Ni on the hydrogen adsorption energy barrier on Co sites. Compared with pristine CoP, the hydrogen adsorption energy barrier of Co sites in Ni-CoP is reduced by 0.41 eV, which means that heteroatom Ni can promote HER kinetics by adjusting the key step energy barrier (Figure 4d).

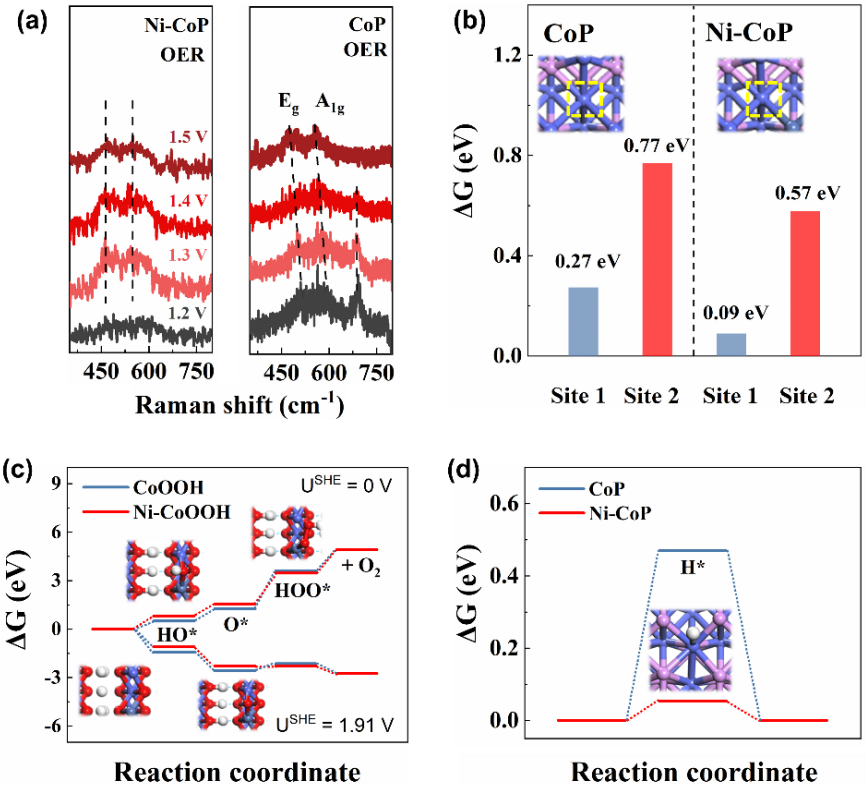

Figure 4. a) In-situ Raman spectrum for Ni-CoP and CoP collected under multi-potential steps. b) Formation free energy of vacancy P in alkaline environment. Gibbs free energy along the reaction steps for: c) OER and d) HER.

3. Conclusion

To summarize, CoP-based catalyst with quasi-covalent bonding mode is prepared through a hydrothermal-phosphating strategy, which is used as a catalytic model. Compared with noble metal catalysts, it demonstrated excellent water electrolysis efficiency (overpotential 1.59 V) and stability in a two-electrode system (current density 100 mA cm^{-2} for 100 h). Theoretical calculations and in situ spectroscopy characterizations indicate that CoP-based catalysts undergo a deeper configuration evolution process in OER compared to HER: Based on the lower *OH adsorption/proton desorption energy barrier provided by DFT calculations and AIMD diagram, P vacancies and transition state Co-O_X caused by PO_X coordination and broken Co-P bond are identified as an important initial reconstruction process. At higher anode potentials, the above configurations follow the reconstruction path guided by the lattice oxygen mechanism of traditional transition metal oxides, which is mainly shown as cobalt-based oxyhydroxides and superoxides. The influence of heteroatom Ni on reconstruction behavior and water splitting performance of the original CoP configuration is analyzed through DFT calculations, which exhibit promoted configuration evolution and reaction kinetics by providing lower P vacancy formation energy and key intermediate adsorption energy barrier. This work provide an intuitive strategy to observe complex structural evolution process, and offer an novel understanding toward the correlation among structure-composition-activity.

4. Experimental Method

4.1. Reagents and chemicals

Potassium hydroxide (KOH) was purchased from Shanghai Sinopharm Chemical Reagent Co. Carbon cloth (CC), cobalt nitrate hexahydrate ($Co(NO_3)_2{\cdot}6H_2O$), Nickel nitrate hexahydrate ($Ni(NO_3)_2{\cdot}6H_2O$), Iron nitrate nonahydrate ($Fe(NO_3)_3{\cdot}9H_2O$), Chromium nitrate nonahydrate ($Cr(NO_3)_3{\cdot}9H_2O$), ammonium fluoride (NH_4F), urea ($CO(NH_2)_2$), Sodium hypophosphite (NaH_2PO_2), Ruthenium oxide (RuO_2) and Platinum-carbon (Pt/C) were obtained from Sigma Aldrich. The ultrapure deionized (DI) water with (18.25 MΩ cm^{-1}) was purified through a Millipore system. In note, the purity of the above reagents is analytical grade, which does not require further purification.

4.2. Synthesis of Co(OH)F/CC and metal doped Co(OH)F/CC precursor

Co(OH)F and metal doped Co(OH)F nanowire precursor were prepared on CC by hydrothermal method. First, the CC (2 × 3 cm^2) was immersed in nitric acid (HNO_3) for 24 hours, aiming to improve hydrophilicity and optimize the hydrothermal growth process. Subsequently, the CC was washed with ethanol and deionized water for 5 min, which was used to grow the precursor. Second, $Co(NO_3)_2{\cdot}6H_2O$ (1 mmol), NH_4F (4 mmol) and $CO(NH_2)_2$ (5 mmol) were mixed by 20 mL of DI water and stirred for 20 min. Furthermore, the CC and precursor solution were sealed into a 25 ml Teflon-lined stainless-steel autoclave, which was used to obtain Co(OH)F/CC nanowire precursors. The preparation process of metal doped Co(OH)F was similar to that of Co(OH)F, transition metal nitrates (0.1 mmol $Ni(NO_3)_2{\cdot}6H_2O$, $Fe(NO_3)_3{\cdot}9H_2O$ and $Cr(NO_3)_3{\cdot}9H_2O$) were added to the precursor solution mentioned above, which also results in the formation of metal doped Co(OH)F nanowires (Metal = Ni, Fe, Cr). The Teflon-lined stainless-steel autoclave containing precursor solution was placed in a hydrothermal environment, which was controlled at 120 for 6 hours.

4.3. Synthesis of CoP/CC, metal doped CoP and commercial catalysts

The nanowire precursors obtained from the hydrothermal solution were washed with deionized water and ethanol, which were dried in a vacuum environment for 5 h. The precursors and 1 g NaH_2PO_2 were put in two quartz boats and placed in a tubular furnace, which was heated to 300 with suitable heating rate (2 /min) in Ar_2 atmosphere (80 sccm) for 2 hours after gas washing process. For the configuration process of commercial catalytic ink, 6 mg RuO_2 and 6 mg Pt (20 ωt%)/C (80 ωt%) catalyst was placed in 1 ml isopropanol solution. Subsequently, the above solution was placed in an ultrasonic cleaning machine and

fully dissolved for 1 hour. This was achieved by dropwise addition of Nafion solution (15 μl) and ultrasonic process (5 min) to obtain commercial catalytic ink. Finally, commercial catalytic ink was dripped onto the CC surface (2 × 3 cm^2), which was subsequently used to compare the performance differences between Co based catalysts and commercial catalysts.

4.4. Synthesis of Ni-CoP/CC with different Ni doping amounts

Ni-CoP/CC with different Ni doping amounts were prepared by above similar processes. Differently, 0.15 mmol or 0.2 mmol $Ni(NO_3)_2{\cdot}6H_2O$ was added to the $Co(NO_3)_2.6H_2O$ precursor solution, which to obtain Ni-CoP nanowire through a hydrothermal-phosphating process.

4.5. Structural characterizations

The morphology of the samples was observed by SEM JEOL S-4800 using an accelerating voltage of 10 kV and TEM JEM-F200 using an accelerating voltage of 80 kV, which were shown in SEM, TEM, HRTEM, SAED and HAADF images. Furthermore, the preferred growth orientation and crystallinity of the samples were shown by the XRD images provided by the Bruker D8 Advance X-ray diffractometer applying Cu Kα radiation (λ = 0.154 nm). The element distribution/composition and electron population were characterized by TEM mapping, EDS, soft XAS and XPS. Among them, the photoemission end-station (BL10B beamline) of soft XAS was located at the in the National Synchrotron Radiation Laboratory (NSRL) in Hefei, China. In addition, the soft XAS data was normalized by the μ(E) energy mode in Athena software. The device model for XPS has been selected as ESCALAB250Xi with Mg Kα (1486.6 eV) as the radiation source. In addition, the catalyst used to test the potential-dependent quasi-in-situ XPS needs to be pretreated for 8 min under the corresponding potential environment.

4.6. Electrochemical measurements

For HER/OER, the electrochemical workstation CHI 660e (Shanghai Chenhua Co., China) was used to collect the electrochemical properties of various catalysts in traditional three electrode systems and alkaline environments (1 M KOH). Among them, the electrocatalyst, Hg/HgO, and Pt sheet in the three electrode system were used as the working electrode (1 × 0.5 cm^2), reference electrode and counter electrode, respectively. Please note that the customized reference electrode in in-situ Raman and CV systems was used to study the surface electrochemical reconstruction process, which was selected as the customized Ag/AgCl. In addition, during the pre-testing phase, the Hg/HgO electrode and Ag/AgCl electrode were calibrated at room temperature. The potentials versus Hg/HgO and Ag/AgCl reference electrode were converted to reversible hydrogen electrode (RHE): $E_{RHE} = E_{Hg/HgO} + 0.098 + 0.059 \times pH$ and $E_{RHE} = E_{Ag/AgCl} + 0.1971 + 0.059 \times pH$. The PH value of 1 M KOH was determined to be 13.5 by PH device. In note, HER and OER data were corrected through 90 % IR compensation, aiming to accurately obtain the intrinsic activity of the catalyst. For HER, CV curve was obtained by the scan rate of 100 mV s^{-1} for 60 cycles between -0.5 and -2.0 V vs Hg/HgO for activating catalysts before the LSV test. Similarly, CV test was obtained by the scan rate of 100 mV s^{-1} for 60 cycles between 0 and 1.2 V vs Hg/HgO for activating catalysts before the LSV test for OER. In detail, LSV curves were selected by a scan rate of 1 mV s^{-1}, the other parameters of LSV test (such as potential range, etc.) were consistent with the activation process. For HER, CV curves at different scan rate between -0.75 and -0.85 V vs Hg/HgO were used to calculate ECSA, which were selected as 20 mV s^{-1}, 40 mV s^{-1}, 60 mV s^{-1}, 80 mV s^{-1} and 100 mV s^{-1}. Similarly, CV curves at different scanning rate (2 mV s^{-1}, 4 mV s^{-1}, 6 mV s^{-1}, 8 mV s^{-1} and 10 mV s^{-1}) between 0.22 and 0.32 V vs Hg/HgO were used to calculate electrochemical active surface area (ECSA) for OER. Furthermore, the LSV curve was normalized by the double layer capacitance obtained from CV data. The relationship between the logarithmic form of current density and overpotential was used to fit the Tafel slope. For overall water splitting, the catalyst grown on CC was used as the cathode and anode in two electrode system to study the electrocatalytic performance. Considering the complex electrolyte environment of overall water splitting in chemical industry, the electrochemical signal of overall water splitting has not been calibrated by the IR compensation process. The charge transport behavior on the catalyst surface was studied by electrochemical impedance spectroscopy (EIS). Among them, the application potentials in HER and OER processes were set to -1.1 V and 0.63 V vs

Hg/HgO, respectively. The frequency range and amplitude for EIS testing were selected to be 0.01 ~ 1x10^5 Hz and 0.005 V. For HER/OER, the stability of the catalyst was estimated in multiple current densities over a short period of time. Besides, for overall water splitting, the stability measurements (i-t) were recorded at constant current density (10 and 100 mA cm^{-2}) for 100 h to evaluate the stability of electrocatalysts.

4.7. Potential and time-dependent in situ Raman spectroscopy

The electrochemical workstation (CHI 660E) and confocal Raman spectrometer (LabRAM HR Evolution) were used to study the in-situ reconstruction phenomenon of catalysts in the HER/OER process. This was mainly divided into two schemes: time-dependent in-situ Raman spectroscopy and potential dependent in-situ Raman spectroscopy. The wavelength and power of the laser source were controlled at 532 nm and 5.36 mW, respectively. The propagation direction of the laser was perpendicular to the working electrode. The acquisition time and accumulation parameters were set to 20 s and double integral mode. In note, unlike traditional electrochemical testing, the catalyst does not need to be activated before in-situ Raman testing, which helps to directly reflect reconstruction process in the initial reaction stage. In addition, all in situ Raman data were collected in stability tests at various application potentials. In situ Electrolytic cell system consists of working electrode (sample), reference electrode (Ag/AgCl), counter electrode (Pt wire), electrolyte solution (1M KOH). Other specific parameters related to specific reaction processes will be discussed in the future, including interval time and application potential.

4.8. Simulation details

The CASTEP code in Materials studio was used to simulate the electronic structure and Gibbs free energy path of the catalytic model. The generalized gradient approximation proposed by Perdew, Burke, and Ernzerhof (GGA-PBE) was identified as the exchange correlation potential. In addition, ultrasoft pseudopotentials are used in the simulation process. The cut-off energy and MonkhorstPack mesh k-point were controlled to be 500.00 eV and 1 x 1 x 1, respectively. Convergence tolerance was considered to be an important parameter in the geometric optimization process, which mainly includes the following aspects: energy factor (5 x 10^{-6} eV per atom), maximum displacement (5 x 10^{-4} A) and maximum force (0.01 eV A^{-1}). The DFT dispersion correction (DFT-D) was used to further analyze the electronic information of the catalyst model, which also considered the van der Waals interaction to improve the reliability of the simulation results. The CoP (011) and CoOOH (010) plane were used to further analyze the adsorption-desorption process and reaction pathways in the HER and OER processes. CP2K/Quickstep code was used for AIMD calculation. The exchange-correlation potential and pseudopotentials were set the same as in Materials Studio. The cutoff energy and van der Waals interactions were also considered, which were selected as 400 eV and DFT dispersion correction (DFT-D3) respectively in this module. The acquisition method of The AIMD simulations was determined to be canonical (NVT) ensemble. Among them, the target temperature and time step were set to 298.15 K and 1.0 fs, respectively.

Acknowledgements

The authors acknowledge the National Natural Science Foundation of China (12025503, U23B2072, 12105208). The authors would like to acknowledge the beamline BL10B at National Synchrotron Radiation Laboratory. The authors acknowledge the Super-computing Center of Wuhan University and University of Science and Technology of China for the numerical calculations support. The authors also acknowledge the Center for Electron Microscopy at Wuhan University for their substantial supports to JEM-F200. The authors acknowledge the open subsidies for large-scale instruments and equipment at Wuhan University.

Conflict of Interest

The authors declare no conflict of interest.

Data Availability

Research data are not shared.

Supporting Information

Supporting Information is available from the Wiley Online Library or from the author.

References

[1] N. Dubouis, D. Ayme-Perrot, D. Degoulange, A. Grimaud, H. Girault, Joule 2024, https://doi.org/10.1016/j.joule.2024.02.012.

[2] Q. Liang, Q. Li, L. Xie, H. Zeng, S. Zhou, Y. Huang, M. Yan, X. Zhang, T. Liu, J. Zeng, K. Liang, O. Terasaki, D. Zhao, L. Jiang, B. Kong, ACS Nano 2022, 16, 7993-8004.

[3] L. Chong, G. Gao, J. Wen, H. Li, H. Xu, Z. Green, J. D. Sugar, A. J. Kropf, W. Xu, X. M. Lin, H. Xu, L. W. Wang, D. J. Liu, Science 2023, 380, 609-616.

[4] X. Wang, S. Xi, P. Huang, Y. Du, H. Zhong, Q. Wang, A. Borgna, Y. W. Zhang, Z. Wang, H. Wang, Z. G. Yu, W. S. V. Lee, J. Xue, Nature 2022, 611, 702-708.

[5] P. Cui, T. Wang, X. Zhang, X. Wang, H. Wu, Y. Wu, C. Ba, Y. Zeng, P. Liu, J. Jiang, ACS Nano 2023, 17, 22268-22276.

[6] Y. Li, W. Wang, M. Cheng, Y. Feng, X. Han, Q. Qian, Y. Zhu, G. Zhang, Adv. Mater. 2023, 35, 2206351.

[7] F. Y. Chen, Z. Y. Wu, Z. Adler, H. Wang, Joule 2021, 5, 1704-1731.

[8] Y. He, F. Yan, X. Zhang, C. Zhu, Y. Zhao, B. Geng, S. Chou, Y. Xie, Y. Chen, Adv. Energy Mater. 2023, 13, 2204177.

[9] W. Zhai, Y. Chen, Y. Liu, T. Sakthivel, Y. Ma, Y. Qin, Y. Qu, Z. Dai, ACS Nano 2023, 17, 17254-17264.

[10] X. Wang, X. Xu, Y. Nie, R. Wang, J. Zou, Adv. Sci. 2023, 10, 2301961.

[11] H. Wu, Z. Wang, Z. Li, Y. Ma, F. Ding, F. Li, H. Bian, Q. Zhai, Y. Ren, Y. Shi, Y. Yang, Y. Deng, S. Tang, X. Meng, Adv. Energy. Mater. 2023, 13, 2300837.

[12] D. He, X. Song, W. Li, C. Tang, J. Liu, Z. Ke, C. Jiang, X. Xiao, Angew. Chem. Int. Ed. 2020, 59, 6929-6935.

[13] L. Gao, C. Tang, J. Liu, L. He, H. Wang, Z. Ke, W. Li, C. Jiang, D. He, L. Cheng, X. Xiao, Energy. Environ. Mater. 2021, 4, 392-398.

[14] L. Fu, J. Zhou, Z. Zhou, B. Xiao, N. Khaorapapong, Y. Kang, K. Wu, Y. Yamauchi, ACS Nano 2023, 17, 22744-22754.

[15] Y. Li, X. Yu, J. Gao, Y. Ma, Chem. Eng. J. 2023, 470, 144373.

[16] Y. Gao, S. Qian, H. Wang, W. Yuan, Y. Fan, N. Cheng, H. Xue, T. Jiang, J. Tian, Appl Catal B-Environ. 2023, 320, 122014.

[17] L. Zhang, J. Zhang, J. Fang, X. Y. Wang, L. Yin, W. Zhu, Z. Zhuang, Small 2021, 17, 2100832.

[18] H. Wang, Y. Wang, J. Zhang, X. Liu, S. Tao, Nano Energy 2021, 84, 105943.

[19] Y. Zhang, Z. X. Hui, H. Y. Zhou, S. F. Zai, Z. Wen, J. Li, C. C. Yang, Q. Jiang, Chem. Eng. J. 2022, 429, 132012.

[20] S. F. Hung, Y. Zhu, G. Q. Tzeng, H. C. Chen, C. S. Hsu, Y. F. Liao, H. Ishii, N. Hiraoka, H. M. Chen, ACS Energy Lett. 2019, 4, 2813-2820.

[21] D. Xu, S. Liu, M. Zhang, L. Xu, H. Gao, J. Yao, Small 2023, 19, 2300201.

[22] X. Zheng, B. Zhang, P. D. Luna, Y. Liang, R. Comin, O. Voznyy, L. Han, F. P. Garcia de Arquer, M. Liu, C. T. Dinh, T. Regier, J. J. Dynes, S. He, H. L. Xin, H. Peng, D. Prendergast, X. Du, E. H. Sargent, Nat. Chem. 2018, 10, 149-154.

[23] X. Ding, H. Huang, Q. Wan, X. Guan, Y. Fang, S. Lin, D. Chen, Z. Xie, J. Energy Chem. 2021, 62, 415-422.

[24] T. Liu, X. Ma, D. Liu, S. Hao, G. Du, Y. Ma, A. M. Asiri, X. Sun, L. Chen, ACS Catal. 2017, 7, 98-102.

[25] Y. N. Zhou, W. H. Hu, Y. N. Zhen, B. Dong, Y. W. Dong, R. Y. Fan, B. Liu, D. P. Liu, Y. M. Chai, Appl Catal B-Environ. 2022, 309, 121230.

[26] J. Y. Xie, Z. Z. Liu, J. Li, L. Feng, M. Yang, Y. Ma, D. P. Liu, L. Wang, Y. M. Chai, B. Dong, J. Energy. Chem. 2020, 48, 328-333.

[27] G. Zhou, M. Li, Y. Li, H. Dong, D. Sun, X. Liu, L. Xu, Z. Tian, Y. Tang, Adv. Funct. Mater. 2020, 30, 1905252.

[28] K. Wu, K. Sun, S. Liu, W. C. Cheong, Z. Chen, C. Zhang, Y. Pan, Y. Cheng, Z. Zhuang, X. Wei, Y. Wang, L. Zheng, Q. Zhang, D. Wang, Q. Peng, C. Chen, Y. Li, Nano Energy 2021, 80, 105467.

[29] H. Song, M. Wu, Z. Tang, J.S. Tse, B. Yang, S. Lu, Angew. Chem. Int. Ed. 2021, 60, 7234-7244.

[30] Y. Sun, W. Sun, L. Chen, A. Meng, G. Li, L. Wang, J. Huang, A. Song, Z. Zhang, Z. Li, Nano Res. 2023, 16, 228-238.

[31] Z. Dai, X. Du, X. Zhang, J. Alloys Compd. 2023, 946, 169451.

[32] H. Yang, Z. Zhou, H. Yu, H. Wen, R. Yang, S. Peng, M. Sun, L. Yu, J. Colloid Interface Sci. 2023, 636, 11-20.

[33] S. Sk, R. Madhu, D. S. Gavali, V. Bhasin, R. Thapa, S. N. Jha, D. Bhattacharyya, S. Kundu, U. Pal, J. Mater. Chem. A. 2023, 11, 10309-10318.

[34] A. Moysiadou, S. Lee, C. S. Hsu, H. M. Chen, X. Hu, J. Am. Chem. Soc. 2020, 142, 11901-11914.

[35] Y. Hu, C. Hu, A. Du, T. Xiao, L. Yu, C. Yang, W. Xie, Anal. Chem. 2023, 95, 1703-1709.

[36] Z. Chen, L. Cai, X. Yang, C. Kronawitter, L. Guo, S. Shen, B. E. Koel, ACS Catal. 2018, 8, 1238-1247.

[37] W. H. Lee, M. H. Han, Y. J. Ko, B. K. Min, K. H. Chae, H. S. Oh, Nat. Commun. 2022, 13, 605.

[38] N. Yao, G. Wang, H. Jia, J. Yin, H. Cong, S. Chen, W. Luo, Angew. Chem. Int. Ed. 2022, 61, e202117178.

ToC figure

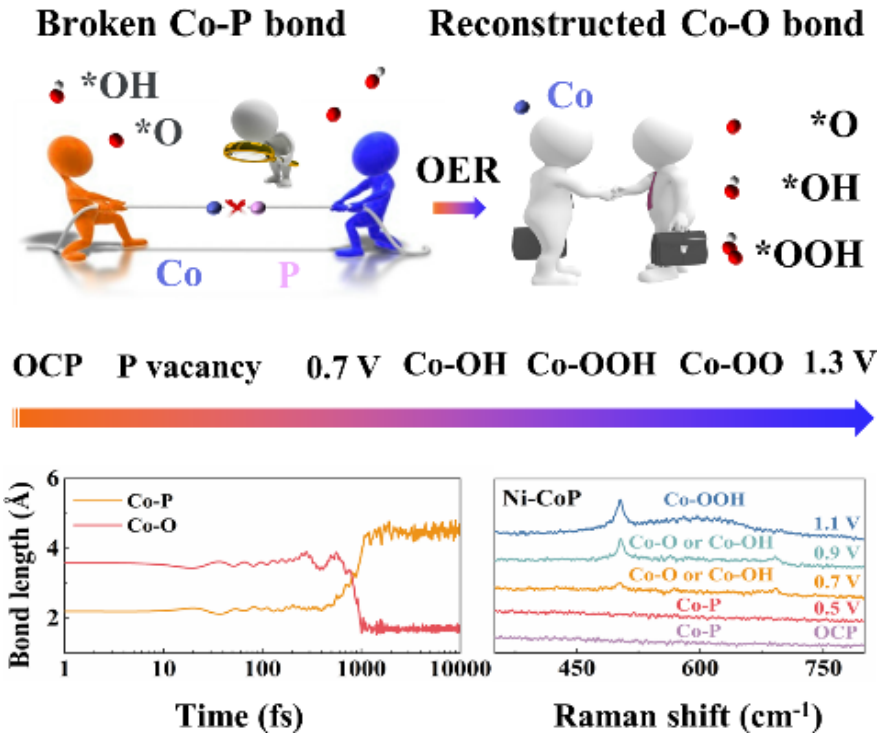

The atomic-level reconstruction behavior of CoP in the oxygen evolution reaction are revealed by molecular dynamics simulation and in situ characterization, mainly including: broken Co-P and reconstructed Co-O species. The fast reconstruction behavior and reaction kinetics of CoP catalysts are realized by heteroatomic Ni, which originate from the lower P vacancy formation energy and rate-limiting step energy barriers.